Nano Research

Open Access

Research Article

Highly efficient transfer hydrogenation of furfural over Co catalysts at ultra-low loading

Jiang Li[§] ✉, Xiaojing Wang[§], Zhidong An[§], Tong Wan, Jiaxing Liu, Junjie Zhang, and Zhenxing Li ✉

State Key Laboratory of Heavy Oil Processing, College of New Energy and Materials, China University of Petroleum (Beijing), Beijing 102249, China

[§] *Jiang Li, Xiaojing Wang, and Zhidong An contributed equally to this work.*

Cite this article: *Nano Research*, **2026**, *19*, 94908390. https://doi.org/10.26599/NR.2026.94908390

ABSTRACT: An ultra-low loading (0.08 wt.%) cobalt single-atom catalyst, synthesized by the adsorption of trace amounts of cobalt salt onto a zeolitic imidazolate framework-8 (ZIF-8) precursor, followed by pyrolysis under Ar at 800 °C, exhibits exceptional performance in the catalytic transfer hydrogenation of furfural to furfuryl alcohol. Under optimized conditions (120 °C, 6 h), the catalyst achieved complete furfural conversion and a selectivity of 96.5% toward furfuryl alcohol. Remarkably, its turnover frequency (TOF) reached 1290.6 h^{-1}, which is three to four orders of magnitude higher than that of previously reported single Co catalysts. The superior catalytic activity is attributed to the uniformly dispersed Co-N_4 matrix and abundant weak and moderate acid sites. Furthermore, Co-ZIF-8-800 exhibited broad substrate scope via the Meerwein–Ponndorf–Verley (MPV) mechanism. This work provides a promising strategy for designing low-cost and highly efficient non-noble metal catalysts for the conversion of biomass-derived platform molecules.

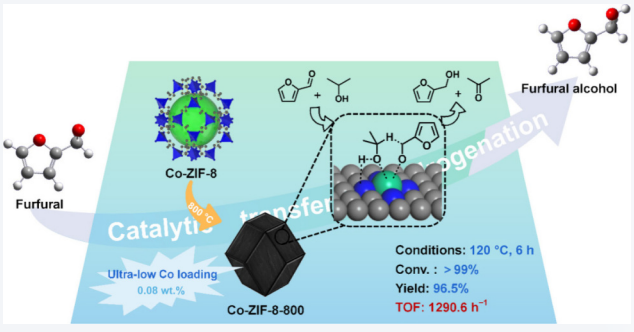

KEYWORDS: biomass, catalytic transfer hydrogenation, zeolitic imidazolate framework-8 (ZIF-8), single-atom, turnover frequency (TOF)

1 Introduction

Tackling climate change and pollution from heavy fossil fuel use is urgent, driving the development of sustainable and clean energy alternatives [1–4]. Furfural (FF) has attracted significant attention as one of the most promising biomass-derived platform molecules to prepare biofuels or value-added chemicals. It is almost the only commercially available unsaturated organic compound derived from carbohydrate feedstocks [5], with versatile functional groups enabling reactions like hydrogenation and oxidation [6]. Current global production of FF is approximately 300,000 tons per year, with about 65% dedicated to the production of furfuryl alcohol (FFA) [7], which has broad industrial applications in polymers, biofuels, and fine chemicals [8, 9]. Catalytic transfer hydrogenation (CTH) utilizes hydrogen donors to replace molecular hydrogen, addressing challenges in the storage, transportation, and safety of fossil-derived H_2, and has emerged as a promising alternative for FF hydrogenation. Noble metal catalysts (e.g., Pt [10], Pd [11], and Ru [12]), non-noble metal catalysts (e.g., Ni [13], Fe [9, 14], and Co [15–18]), and various solid acid/base catalysts [19, 20] have made significant progress in enhancing catalytic efficiency and selectivity in CTH reactions. However, challenges remain, as the high cost and scarcity of noble metals limit industrial application, while non-noble metal catalysts often suffer from insufficient activity, selectivity, or stability. Thus, developing efficient and cost-effective non-noble metal catalysts is crucial.

In recent years, cobalt-based catalysts have attracted significant attention for biomass conversion, including the CTH of FF to FFA [21]. Li et al. developed a magnetic CoO@C catalyst through a carbon coating strategy, which effectively mitigated the agglomeration of cobalt particles at elevated temperatures, exhibiting enhanced catalyst stability and activity [16]. The optimized performance of this catalyst was observed at a high temperature of 180 °C, resulting in an FFA selectivity of 99.2% at an FF conversion of 91.5%. Such high operating temperature significantly increases energy consumption and limits the sustainability of the process. Although carbon coating can suppress

Received: October 17, 2025; **Revised:** December 24, 2025
Accepted: December 30, 2025

✉Address correspondence to Jiang Li, lijiang@cup.edu.cn; Zhenxing Li, lizx@cup.edu.cn

cobalt agglomeration, it may also obstruct the exposure of active sites, thereby reducing the utilization efficiency of metal atoms. Lu et al. leveraged the synergistic effect of abundant N-anchoring sites and the hierarchical porosity of biomass-derived nitrogen-doped carbon (NC) to confine Co_3O_4 nanoparticles, yielding highly dispersed Co_3O_4@NC catalysts [17]. The catalyst achieved an FF conversion of 98.7% and an FFA selectivity of 97.1% at 160 °C in 6 h. However, the system still relies on high-pressure hydrogen and thus does not constitute a pure CTH process, fundamentally remaining constrained by the limitations of conventional hydrogenation. Cristina et al. synthesized Co_3O_4-Al_2O_3 with a composite structure, which provided acidic and basic sites essential for the Meerwein–Ponndorf–Verley (MPV) reduction during CTH [22]. At 150 °C, the catalyst achieved an FFA yield of 74% in 6 h, but a higher yield of 92% required 24 h, which limits industrial feasibility and efficiency. To sum up, the relatively low catalytic activity of cobalt means that it is more likely to be employed alongside other metals (e.g., Ni and Ru) as co-catalysts in bimetallic alloys, or within composite/core–shell architectures rather than as a standalone metal center [22–25]. For example, Wang et al. embedded Co-Ni alloy nanoparticles into a UiO-66-NH_2 framework using a laser-assisted solvent incorporation method [23]. Under mild conditions (1 bar N_2, 130 °C), the catalyst achieved an FF conversion of 94.3% with an FFA selectivity of 100% after 6 h. The outstanding performance was attributed to dual-metal synergy and efficient charge transfer at the active sites. Nevertheless, such reliance on dual-metal synergy and complex architectures obscures the intrinsic catalytic role of cobalt and hampers mechanistic understanding. Therefore, the development of cobalt-based catalysts is currently limited by two critical bottlenecks: Single-metallic Co catalysts generally require harsh reaction conditions and exhibit low intrinsic activity [15–18], whereas bimetallic or composite Co systems, despite improved performance, suffer from increased structural complexity, unclear synergistic effects, and difficulty in identifying the intrinsic role of cobalt [25–28]. Finally, many studies do not provide a thorough investigation of the intrinsic activity of catalysts, such as site-specific activity and turnover frequency (TOF), which hampers the data comparability and accurate assessments of catalyst performance across different studies.

To overcome the intrinsic activity–stability trade-off in cobalt catalysis, single-atom catalysts (SACs) have emerged as a promising strategy, owing to their maximized atomic utilization, atomically dispersed and well-defined active sites, and superior capability for selectivity regulation [29, 30]. However, the development of Co-based SACs faces distinct challenges. Co is more prone to migration and aggregation at high temperatures during both the preparation and reaction processes, which hinders the stabilization of isolated atoms and often leads to cluster or nanoparticle formation [31]. To address this issue, strategies such as spatial confinement, coordination site construction, and defect engineering have been proposed [32–35]. Recently, we developed a single-atom iron catalyst (SA-Fe) with an exceptionally low iron loading of less than 0.1 wt.% via a saturation adsorption strategy from zeolitic imidazolate framework-8 (ZIF-8) precursor [14]. Building on this approach, we successfully established an ultra-low metal-loading Co-ZIF-8-800 catalyst (0.08 wt.%), which achieves atomic dispersion of Co and exhibits excellent catalytic performance for the CTH of FF to FFA using 2-propanol (2-PrOH) as the hydrogen donor. We systematically examined the performance of various Co catalysts derived from different metal-organic framework (MOF) precursors, including Co-based MOFs such as ZIF-67 and Zn-based MOFs like MOF-5 and ZIF-8. Although ZIF-67 can directly afford Co catalysts after pyrolysis, the large Co nanoparticles (NPs) and incompatible acidity lead to unsatisfactory performance, while only a conversion of 9.1% and a selectivity of 36.3% were achieved under identical reaction conditions. By comparison, the Co-ZIF-8-800 catalyst displayed the best catalytic activity and selectivity, achieving an FF conversion of 100% and an FFA selectivity of 96.5% at 120 °C in 6 h, which is comparable to those of state-of-the-art catalysts. This exceptional performance is attributed to the uniformly dispersed Co-N_4 matrix and abundant weak and moderate acid sites. Additionally, the catalyst gave a TOF of 1290.6 h^{-1} at 120 °C, which is three to four orders of magnitude higher than those of single Co catalysts in previous reports.

2 Experimental

2.1 Chemicals

Cobalt nitrate hexahydrate (99.9%), alcohols, and N,N-dimethylformamide (99.5%) were purchased from Sinopharm Chemical Reagent Co., Ltd. FF (98.0%), FFA (97.0%), 4-fluorobenzaldehyde (98.0%), 4-fluorobenzyl alcohol (98.0%), 4-chlorobenzaldehyde (97.0%), 4-chlorobenzyl alcohol (99.0%), 4-(trifluoromethyl)benzaldehyde (95.0%), 4-[(trifluoromethyl)phenyl] methanol (96.0%), 4-tert-butylbenzaldehyde (95.0%), 4-tert-butylbenzyl alcohol (97.0%), 2-phenethyl alcohol (98.0%), p-phthalic acid (99.0%), benzaldehyde (98.0%), benzyl alcohol (99.0%), and 4-(2-furyl)-3-buten-2-one (98.0%) were purchased from TCI. 2-Methylimidazole (Hmim) (98.0%), 5-hydroxymethylfurfural (99.0%), 2,5-furandimethanol (98.0%), (5-methyl-2-furyl)methanol (97.0%), cinnamaldehyde (98.0%), cinnamic alcohol (98.0%), 2-thiophenecarboxaldehyde (98.0%), 2-thiophenemethanol (98.0%), pyridine-2-carboxaldehyde (98.0%), and 2-pyridinemethanol (98.0%) were purchased from Aladdin Reagent Co., Ltd. Zinc nitrate hexahydrate, phenylacetaldehyde (95.0%), and 5-methyl furfural (99.0%) were purchased from Xiya Reagent Co., Ltd.

2.2 Catalysts preparation

Catalysts were prepared by the pyrolysis of Co-ZIF-8 precursors under Ar at 400–1000 °C. The prepared catalysts were denoted as Co-ZIF-8-*T*, where *T* represents the pyrolysis temperature in Celsius. All Co-ZIF-8 catalysts were synthesized using the following procedure, which adapted the classic room-temperature methanolic synthesis of ZIF-8 [36, 37]. First, zinc nitrate hexahydrate (2790 mg) was added to methanol (100 mL). After the precursor was completely dissolved, 2-methylimidazole (3080 mg) was added to the above solution, followed by the addition of 100 mL of methanol. The mixture was vigorously stirred at room temperature until a white suspension was formed, and then 175 mg of cobalt nitrate hexahydrate was added. The combined mixture was stirred for another 6 h at room temperature. Afterwards, the produced solids were centrifuged at 10,000 r·min^{-1} for 5 min and washed three times with ethanol before being dried overnight in a vacuum at 60 °C. Finally, the mixture was ground into a fine powder and then pyrolyzed in a tubular furnace under an argon flow rate of 100 mL·min^{-1}. To prepare the optimal Co-ZIF-8 catalyst, the temperature program was as follows: 20 °C was held for 60 min, ramped to 800 °C at 5 °C·min^{-1}, and held for 2 h. The catalysts

prepared from different batches exhibited high catalytic reproducibility.

To tune the Co loading, a two-step route was adopted. The ZIF-8 precursor was prepared at first and then pyrolyzed at 800 °C to furnish ZIF-8-800 support. A certain amount of cobalt nitrate hexahydrate was then dissolved in 0.5 mL of methanol, and then dropped onto 300 mg of ZIF-8-800 support. The mixture was held at 70 °C for 1 h to remove the methanol, followed by pyrolysis at 800 °C under the same temperature program as used in the one-step route. Based on our previous study, the two-step route achieved comparable catalytic performance and single-atom metal dispersion to those obtained via the one-step route at the same Co loading [14].

A typical procedure for Co-MOF-5-800 catalyst preparation was as follows: First, zinc nitrate hexahydrate (3.63 g) was added to N,N-dimethylformamide (100 mL). After the precursor was completely dissolved, terephthalic acid (H_2BDC, 3080 mg) was added to the above solution. The solution was vigorously stirred at room temperature for 30 min, and then vigorously stirred at 100 °C until a white mixture formed. Then, 126.3 mg of cobalt nitrate hexahydrate was added. This combined mixture was stirred for 24 h at 100 °C. Afterwards, the produced solids were centrifuged at 10,000 r·min^{-1} for 5 min and washed three times with ethanol before being dried overnight in a vacuum at 60 °C. Then the mixture was ground into a fine powder and pyrolyzed using the same program as for the Co-ZIF-8-800 catalyst.

A typical procedure for ZIF-67-800 catalyst preparation was as follows: First, 0.45 g of cobalt nitrate hexahydrate was dissolved in 3 mL of deionized (DI) water, and 5.5 g of 2-methylimidazole was dissolved in 20 mL of DI water. The two solutions were mixed (Co^{2+}:Hmim:H_2O = 1:58:1100) and stirred at room temperature for 6 h. The resulting purple precipitate was washed three times with water and methanol and finally dried under vacuum at 80 °C for 24 h. Then the mixture was ground into a fine powder and pyrolyzed using the same program as for the Co-ZIF-8-800 catalyst.

2.3 Catalyst characterization

The morphology of the catalysts was characterized using a Hitachi SU8010 scanning electron microscopy (SEM, Japan) at 20 kV. Transmission electron microscopy (TEM), high-angle annular dark-field scanning transmission electron microscopy (HAADF-STEM), and elemental analysis using an energy dispersive X-ray spectroscopy (EDS) were performed on a JEOL JEM-2100F instrument operated at 200 kV. N_2 adsorption measurements were performed on an ASAP2020M adsorption analyzer. X-ray diffraction (XRD) was performed at room temperature on an X-ray diffractometer (TTR-III, Rigaku Corp., Japan) with Cu Kα radiation (λ = 1.54056 Å). The data was recorded at 2θ ranges of 5°–70°. X-ray photoelectron spectroscopy (XPS) measurements were conducted on an XPS instrument (ESCALAB 250Xi, Thermo-VG Scientific, USA) with monochromatic Al Kα radiation (1486.92 eV). The spectra were fitted using mixed Gaussian–Lorentzian component profiles after subtraction of a Shirley background. The full width half maximum (FWHM) was fixed as 1.6 eV. The nitrogen content was determined by the elemental analysis (Eurovector EA 3000). The cobalt and zinc content were determined using inductively coupled plasma-atomic emission spectroscopy (ICP-AES) (Optima 7000DV, PerkinElmer Inc.). NH_3-temperature programmed desorption (NH_3-TPD) was performed as follows: Firstly, approximately 100 mg of sample was loaded in a quartz reactor and then heated at 500 °C under argon flow for 2 h. Then, the adsorption of NH_3 was carried out at 40 °C for 1 h. Subsequently, the catalysts were flushed with argon at 40 °C for 1 h, and then heated to 700 or 800 °C with a ramp rate of 10 °C·min^{-1}. Raman spectra were obtained through a Raman spectrometer (HORIBA Jobin Yvon, France) with λ = 532 nm. Thermogravimetric analysis was accomplished using a thermogravimetric-differential thermal analysis (TG-DTA) analyzer Shimadzu DTA-60 instrument. Under Ar flow, a sample was heated from 30 to 1000 °C with a ramp rate of 10 °C·min^{-1}. For CO adsorption diffuse reflectance infrared Fourier transform spectroscopy (CO-DRIFTS) analysis, 25 mg of catalyst was subjected to *in-situ* pretreatment in 5 vol.% H_2/Ar at 400 °C for 1 h (10 °C·min^{-1} ramp). After cooling to 25 °C and purging with Ar, a background spectrum was acquired. CO adsorption was then carried out in 5 vol.% CO/He for 40 min, followed by Ar purging (15–20 min) and collection of the CO-adsorbed DRIFTS spectrum.

2.4 Experimental procedure for catalyst evaluation

The CTH of FF was carried out using a thick-wall glass tube (15 mL capacity, Synthware). For a typical procedure, FF (0.5 mmol), heterogeneous catalyst (50 mg), and 2-propanol (3 mL) were mixed in a glass tube, and then the mixture was vigorously stirred in a silicon oil bath at 120 °C for 6 h. After the reaction, the liquid products were analyzed using both gas chromatography (GC) and gas chromatography-mass spectrometry (GC-MS). GC-MS analysis was conducted with an Agilent 7890B GC equipped with a DB-WAX 30 m × 0.25 mm × 0.25 μm capillary column (Agilent). The GC was directly interfaced to an Agilent 5977 mass selective detector (EI, 70 eV). The following GC oven temperature programs were used: 40 °C was held for 1 min, ramped to 120 °C at 5 °C·min^{-1}, ramped to 240 °C at 10 °C·min^{-1}, and held for 5 min.

Some experiments were performed at least twice to ensure the reproducibility. The carbon loss is attributed to undetected products in the GC or coke formation. The conversion and yield for the hydrogenation of FF were calculated in mol%, and TOF for CTH was calculated in h^{-1} as follows

$$\text{Conversion} = \left(1 - \frac{\text{Molar amount of FF after reaction}}{\text{Molar amount of FF before reaction}}\right) \times 100\% \quad (1)$$

$$\text{Yield} = \frac{\text{Molar amount of each product after reaction}}{\text{Molar amount of FF before reaction}} \times 100\% \quad (2)$$

$$\text{TOF} = \frac{\text{Molar amount of FF consumed at low conversions}}{\text{Molar amount of Co in catalysts} \times \text{reaction time}} \quad (3)$$

Here, the molar amount of FF consumed at low conversions was determined from the yield of FFA, rather than from the overall FF consumption, to avoid the influence of side reactions and ensure that the calculated consumption corresponds exclusively to the formation of FFA from FF via CTH.

The stability of the Co-ZIF-8-800 catalyst was investigated in five consecutive runs. The used catalyst was separated from the resulting reaction mixture via centrifugation, followed by washes with ethanol three times. After being dried overnight in a vacuum at 60 °C, the catalyst was used directly in the next run. To recover

the activity of the used Co-ZIF-8-800 catalyst, cobalt nitrate hexahydrate in methanol solution (0.01 wt.% Co) was dropped onto 50 mg of the used Co-ZIF-8-800 catalyst. The mixture was then re-pyrolyzed at 800 °C using a similar program as the Co-ZIF-8-800 catalyst, except another 70 °C hold for 1 h to remove the methanol.

3 Results and discussion

3.1 Catalyst synthesis and characterization

The synthesis of Co catalysts from three types of MOF precursors, ZIF-8, ZIF-67, and MOF-5, is illustrated in Fig. 1(a). Using a saturated adsorption strategy as we reported previously [14], the Co-ZIF-8-800 catalyst was prepared at an ultra-low cobalt loading of 0.08 wt.% (detected by ICP-AES analysis) (Table S3 in the Electronic Supplementary Material (ESM)). Accordingly, a highly dispersed Co-N_x matrix is established. The TEM images of Co-ZIF-8-800 (Figs. 1(b) and 1(c)) reveal a well-preserved lamellar structure after pyrolysis. No nanoparticles are observed in aberration-corrected TEM (AC-TEM) (Fig. S1 in the ESM), indicating the absence of metal aggregation. Elemental mapping (Figs. 1(f) and 1(g)) further confirms the homogeneous dispersion of Co species in Co-ZIF-8-800. By comparison, the pyrolysis of Co-MOF-5 and ZIF-67 resulted in the collapse of the initial structure and irregular Co NPs with average diameters of 38.90 and 28.43 nm, respectively (Figs. 1(d) and 1(e)). XRD patterns also revealed differences in the states of zinc and cobalt among these catalysts (Fig. 1(h)). Co-MOF-5-800 exhibited peaks for Zn and metallic cobalt (110) planes. Distinct peaks at 44.2° and 51.5° corresponding to metallic cobalt (111) and (200) planes are observed in ZIF-67-800. Co-ZIF-8-800 displays no diffraction peaks for Co or Zn species. Correspondingly, Co and Zn atoms may be highly dispersed as single atoms, as in our previous study [14]. Raman spectroscopy indicated a higher peak intensity ratio (I_D/I_G = 1.32) for Co-ZIF-8-800, suggesting a lower degree of graphitization, increased disorder in carbon, and more defects (Fig. 1(i) and Table S5 in the ESM).

XPS spectra showed the complete loss of zinc and nitrogen species after pyrolysis at 1000 °C (Figs. S3 and S4 in the ESM). Compared with ZIF-8-800, the slight increase in Zn binding energy in the Co-loaded catalyst suggests possible electron transfer from Zn to Co through the metal-N matrix, even without direct Co–Zn bonding (Fig. 2(e)). This parallels the phenomenon of Zn → Cu electron donation, which has been established in Cu/Zn-NC systems even in the absence of direct Zn–Cu bonds [38].

Given the inability of AC-TEM (Fig. S1 in the ESM) to reliably distinguish Co and Zn atoms owing to their similar atomic numbers, together with the absence of a discernible Co 2p XPS signal at Co loadings below 0.1 wt.% (Fig. S7 in the ESM), X-ray absorption near-edge structure (XANES), extended X-ray absorption fine structure (EXAFS), and wavelet transform (WT) analyses were conducted at the Co and Zn K-edges to probe the oxidation state and local coordination environment of cobalt species in Co-ZIF-8-800 (Fig. 2). As shown in the Co K-edge and Zn K-edge XANES spectra (Figs. 2(a) and 2(b)), the cobalt and znic atoms in Co-ZIF-8-800 are in an oxidation state. The Co K-edge Fourier transform extended XAFS (FT-EXAFS) spectra for Co-ZIF-8-800 (Fig. 2(c)) exhibit a primary peak at 1.50 Å, corresponding to the Co–N coordination. A secondary peak appears at 2.58 Å, suggesting the presence of a heteronuclear Co–Zn interaction in the second coordination shell [39]. Similarly, in the Zn K-edge FT-EXAFS spectrum (Fig. 2(d)), a main peak at 1.47 Å corresponding to Zn–N coordination and a secondary peak at 2.45 Å likely associated with a Co–Zn scattering path are observed. These FT-EXAFS results strongly indicate the presence of an appropriate interatomic distance between the dual-metal atoms, rather than the formation of direct metal–metal bonds. In WT analysis (Fig. 2(e)), no intensity features related to Co–Co scattering is detected in the high k value range, confirming the atomically dispersed nature of the Co species. Similarly, the WT of the Zn K-edge further supports the exclusive presence of Zn–N coordination [40–42]. Quantitative EXAFS fitting reveals a Co–N coordination number of approximately 3.6 (Table S7 in the ESM), indicating the coexistence of Co–N_3 and Co–N_4 coordination environments (Fig. 2(f)). The Zn–N coordination number in Co-ZIF-8-800 is approximately 4.0 (Fig. 2(g) and Table S8 in the ESM), which is comparable to that of pristine ZIF-8-800. CO-DRIFTS spectroscopy further confirmed the uniform distribution of isolated Co–N sites. The absence of CO bridged adsorption in the region of 1870–1840 cm^{-1}, together with the invariant positions of CO linear adsorption peaks on Co (2172 and 2117 cm^{-1}) regardless of CO coverage (Fig. 2(h)), unambiguously confirmed the atomically dispersed nature of isolated Co species on the support [43].

We used NH_3-TPD to explore the acidity of these catalysts (Figs. S8 and S9 in the ESM). ZIF-67-800 exhibited a peak around 450 °C, indicating strong acid sites, which can be attributed to the formation of large Co NP supported on N–C during pyrolysis. In contrast, Co-ZIF-8-800 demonstrated predominant weak and moderate acidic sites as the broad NH_3 desorption peak (70–470 °C). Weak acid sites promote the adsorption and activation of the carbonyl group in FF, while moderate acid sites improve conversion [21]. Conversely, excessively strong acid sites may lead to side reactions [44]. The acidity of Co-ZIF-8-800 originates from the synergistic interplay between Zn–N and Co–N coordination and defect-rich N-doped carbon generated during high-temperature pyrolysis. Among these factors, Zn–N and N–C units are the primary contributors, while Co–N further enhances the overall acidity. In contrast, Co-MOF-5-800 and Co-ZIF-8-1000 display negligible acidity due to the absence of metal–N motifs or the substantial loss of Zn and N, which correlates with their inferior CTH performance.

3.2 Catalyst evaluation and investigation of structure-activity relationship

Table 1, and Fig. S9 and Table S11 in the ESM present the catalytic performance of various catalysts, highlighting the critical roles of the MOF precursor and Co. Trace amounts of FFA were observed in the blank test (Table 1, entry 1). Co species significantly improved the FF conversion and FFA selectivity (Table 1, entries 2–8). Among these, Co-ZIF-8-800 exhibited the best catalytic performance, attributed to its uniformly dispersed Co-N_4 matrix and abundant weak and moderate acid sites as noted above (Table 1, entry 2). Moreover, the linear correlation between the specific reaction rate and Co loading further confirms that the primary active sites are SA-Co species (Fig. 3(b)). The TOF of 1290.6 h^{-1} at 120 °C is 3–4 orders of magnitude higher than that of previously reported single Co catalysts (Fig. 3(a)), successfully overcoming the common low-activity limitation of cobalt as a monometallic center (Table S1 in the ESM), and even surpassing bimetallic Co catalysts like the Co-Ru catalyst (Table S2 in the ESM) [24]. In comparison,

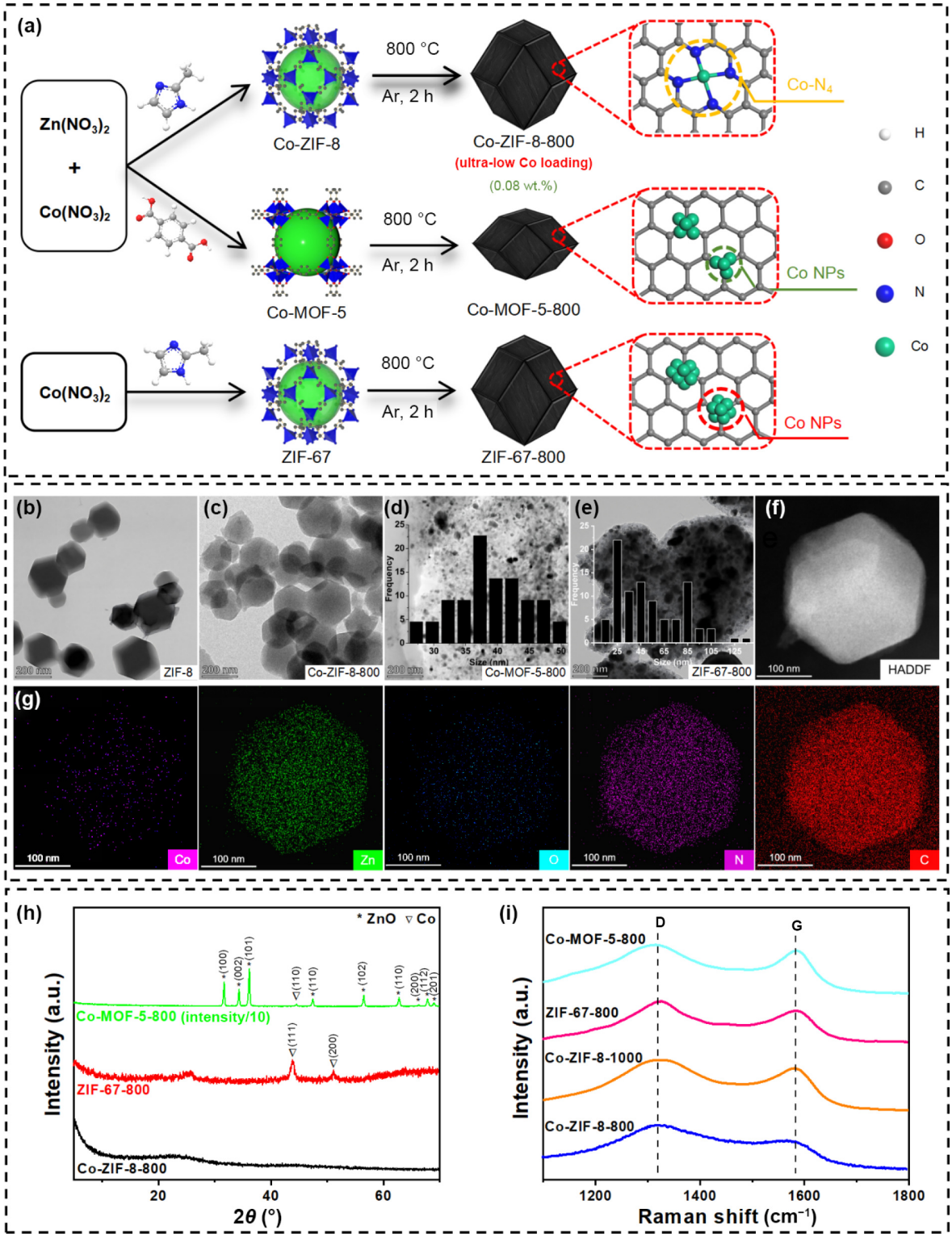

Figure 1 Schematic diagram for catalyst synthesis and multiple characterization data. (a) Schematic diagram for synthesis of Co catalysts using ZIF-8, ZIF-67, and MOF-5 as precursors. TEM images of (b) ZIF-8, (c) Co-ZIF-8-800, (d) Co-MOF-5-800, and (e) ZIF-67-800. (f) HAADF-STEM and (g) Co, Zn, O, N, and C elemental maps of Co-ZIF-8-800. (h) XRD patterns and (i) Raman spectra of cobalt catalysts prepared from different precursors.

Co-MOF-5-800 and ZIF-67-800 exhibit inferior performance due to the large Co NPs and incompatible acidity (Table 1, entries 3 and 4). Using MOF precursors (without pyrolysis) as catalysts led to poor performance (Table S9 in the ESM). When pyrolyzed at 400 °C, the desired C–N structure was not formed (Fig. S2 in the ESM), leading to a relatively high selectivity (87.6%) but low conversion of 10.5% (Table 1, entry 6). By comparison, the pyrolysis at 1000 °C led to the collapse of the ZIF-8 structure and nearly complete loss of nitrogen and Zn atoms (Fig. S2 in the ESM), resulting in lower FFA selectivity and FF conversion than those of Co-ZIF-8-800 catalysts

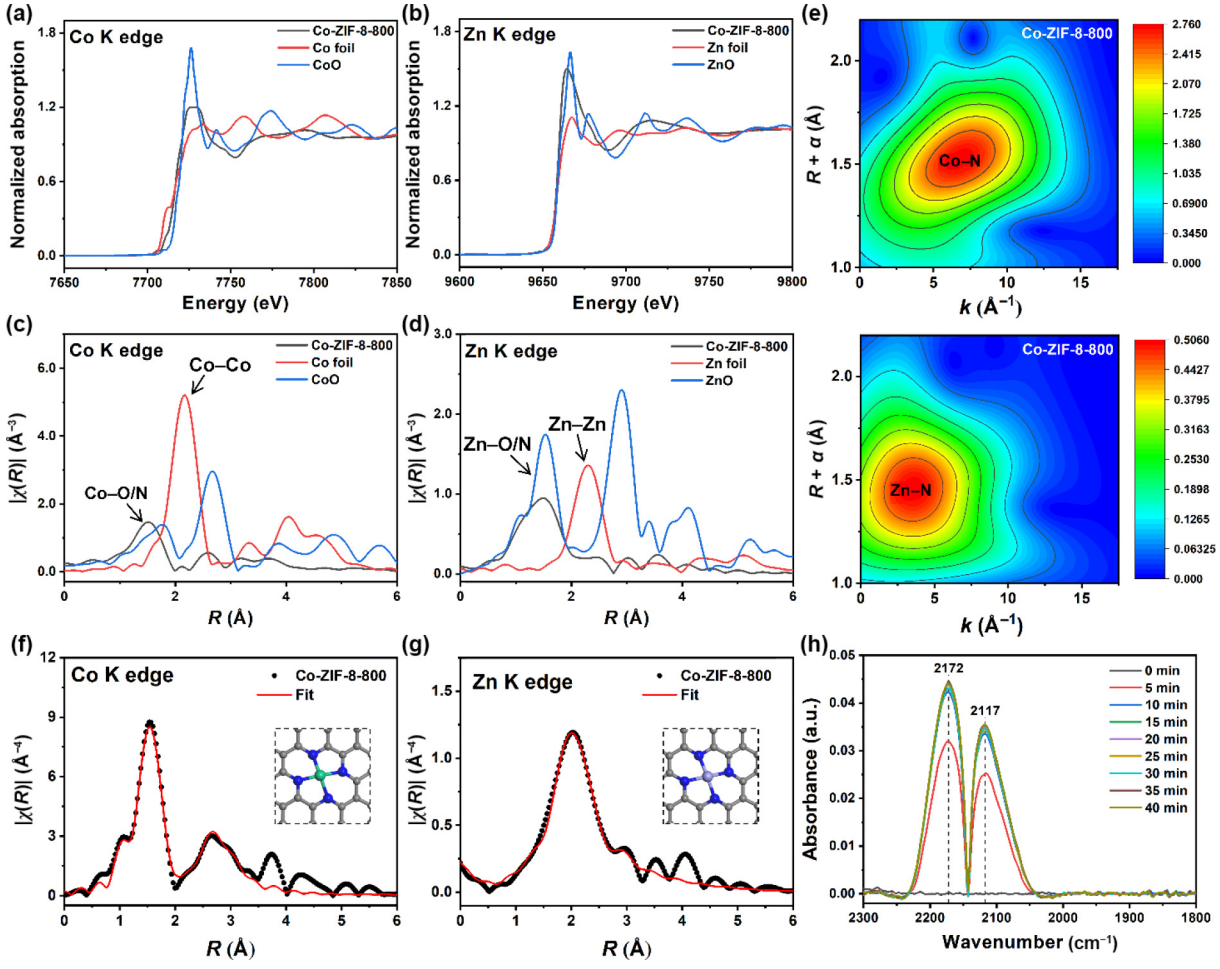

Figure 2 X-ray absorption spectra and analysis. (a) Co K-edge and (b) Zn K-edge XANES spectra. Fourier transforms of (c) k^2-weighted Co K-edge and (d) k^2-weighted Zn K-edge EXAFS spectra. (e) WT of Co K-edge EXAFS for Co-ZIF-8-800 and Zn K-edge EXAFS for Co-ZIF-8-800. ((f) and (g)) EXAFS fitting of the Co-ZIF-8-800 at Co and Zn K-edges. Insets: atomic structure models of Co-ZIF-8-800; Co (green), Zn (light blue), N (blue), and C (gray). (h) Background-subtracted CO-DRIFTS time profile spectra of Co-ZIF-8-800 obtained at room temperature.

Table 1 CTH of FF over various catalysts[a]

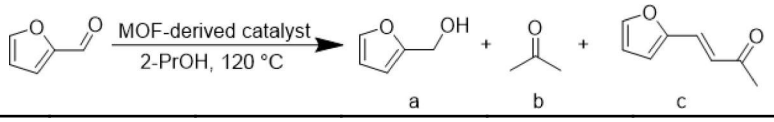

Entry	Catalyst	*t* (h)	Conv. (%)	Yield (%)	Sel. (%)	Yield of solvent-derived products (%)	
						b	c
1	—	6	27.8	2.9	10.4	39.4	< 0.1
2	Co-ZIF-8-800	6	100	96.5	96.5	162.3	0.5
3	Co-MOF-5-800	6	45.3	36.7	81.0	64.7	2.1
4	ZIF-67-800	6	9.1	3.3	36.3	44.7	< 0.1
5	ZIF-8-800	6	22.1	12.0	54.3	22.7	0.4
6	Co-ZIF-8-400	6	10.5	9.2	87.6	9.6	0.2
7	Co-ZIF-8-1000	6	29.2	23.1	79.1	70.9	0.4
8	Ni-ZIF-8-800	6	17.2	1.2	7.2	9.4	< 0.1
9	Cu-ZIF-8-800	6	25.7	6.1	23.9	23.4	< 0.1
10	Pd/C	1	14.8	0.6	4.1	5.8	< 0.1
11	Pt/C	1	16.3	0.7	4.3	3.5	< 0.1
12	Ru/C	1	36.9	27.7	75.1	4.0	< 0.1

[a]Reaction conditions: 0.5 mmol of FF, 3 mL of 2-PrOH, and 50 mg of catalyst (the molar ratio of Co to FF is 0.14% for Co-ZIF-8-800 catalyst).

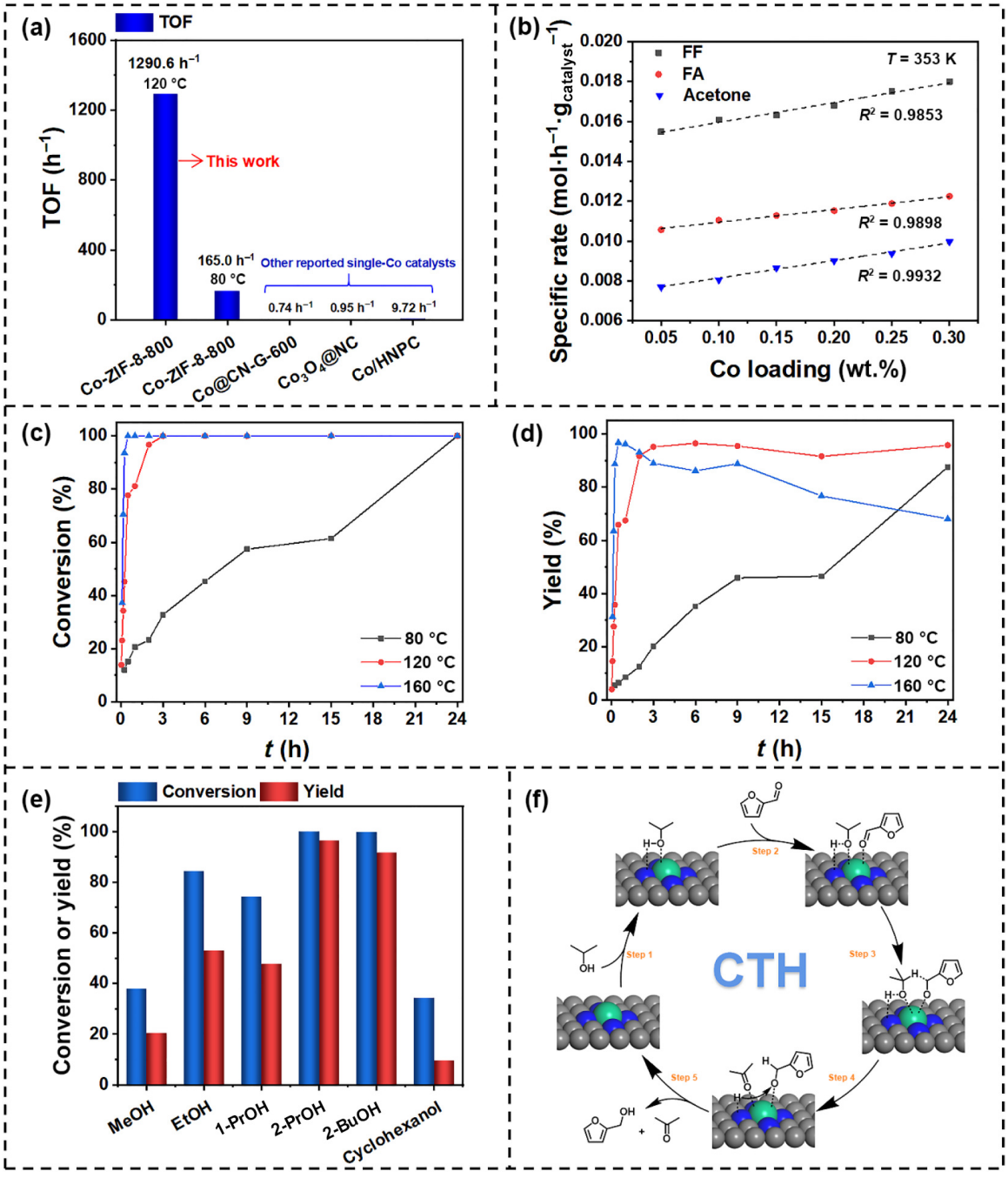

Figure 3 Catalyst performance benchmarking and reaction mechanisms. (a) TOF of various catalysts. (b) Correlation of Co loading with specific reaction rates. Reaction conditions: 0.5 mmol of FF, 50 mg of Co-ZIF-8-800 catalyst, 3 mL of 2-PrOH solvent, 80 °C, and 5 min. ((c) and (d)) Effect of reaction temperature. Reaction conditions: 0.5 mmol of FF, 3 mL of 2-prOH, and 50 mg of Co-ZIF-8-800. (e) Screening of H donor for the CTH of FF over Co-ZIF-8-800. Reaction conditions: 0.5 mmol of FF, 50 mg of Co-ZIF-8-800, 3 mL of solvent, 120 °C, and 6 h. (f) Proposed mechanism for CTH of FF.

(Table 1, entry 7). In addition, other non-noble metal catalysts, such as Ni- and Cu-based systems, exhibit markedly lower FF conversion and FFA selectivity (Table 1, entries 8 and 9), further highlighting the superior catalytic efficiency of the Co-ZIF-8-800 catalyst developed in this work. Common noble metal catalysts like Pd/C, Pt/C, and Ru/C exhibited lower conversion and selectivity under similar conditions (Table 1, entries 10–12). The formation of acetone (dehydrogenation product of 2-PrOH solvent) and (*E*)-4-(furan-2-yl)but-3-en-2-one (coupling by-product of FF and acetone) indicates solvent transformation and side reactions, respectively. The higher yield of acetone compared to FFA (Table 1, entries 2–7) indicates that the catalyst exhibits independent dehydrogenation ability, as evidenced by a linear relationship between Co loading and the specific generation rate of acetone (Fig. 3(b)).

The effects of reaction temperature were evaluated (Figs. 3(c) and 3(d)). At 80 °C, the FF conversion and FFA yield gradually increased with reaction time, achieving complete FF conversion and an FFA selectivity of 87.6% after 24 h. At 120 °C, complete FF conversion was achieved within 6 h, with a peak FFA selectivity of

96.5%. At 160 °C, optimal performance was achieved in only 30 min, with an FF conversion of 100% and an FFA selectivity of 96.8%. Extending the reaction to 24 h, however, the FFA selectivity decreased to 68.1%. The major by-products are aldol condensation products from FF and solvent-derived acetone [24].

To investigate the effect of hydrogen donors, a range of primary and secondary alcohols were tested (Fig. 3(e)). Primary alcohols (MeOH, EtOH, and 1-PrOH) led to low FFA selectivity with low FF conversion. These results can be ascribed to their higher redox potentials and inherently weaker hydrogen-donating capacities, which restrict the formation of active hydride species. In addition, the longer alkyl chains of these alcohols introduce steric hindrance that impedes their effective adsorption on the catalyst surface [16]. In contrast, secondary alcohols such as 2-PrOH exhibited the best CTH performance. Cyclohexanol showed low FFA selectivity because its high viscosity limited effective contact between catalyst and substrate.

The linear correlation between Co loading and specific reaction rate clearly indicates that SA-Co species are the active sites (Fig. 3(b)). Furthermore, the negligible activity of homogeneous cobalt salts (Table S10 in the ESM) together with trace cobalt leaching detected by ICP-optical emission spectroscopy (OES) analysis (Table S12 in the ESM) confirms that the reaction proceeds via a heterogeneous pathway, with the superior catalytic performance originating from atomically dispersed Co–N sites anchored in the carbon matrix. Despite the catalyst's inherent dehydrogenation ability, the markedly lower specific rate of acetone relative to FF or FFA suggests that the transfer hydrogenation is the dominant reaction pathway in this system rather than the conventional dehydrogenation–hydrogenation mechanism. The reaction mechanism was proposed based on the classic MPV mechanism and our previous work (Fig. 3(f)) [14, 21]. Intermolecular hydride transfer through a cooperative six-membered-ring transition state, rather than metal-mediated hydrogenation, was involved in the CTH of FF to FFA over the Co-ZIF-8-800 catalyst. Correspondingly, acetone was generated as a by-product via dehydrogenation of 2-PrOH.

The stability of Co-ZIF-8-800 was tested over five cycles under moderate FF conversion (Fig. S10 in the ESM). The FF conversion significantly declined after the third cycle, while the FFA selectivity remained unchanged. To elucidate the origin of catalyst deactivation, the used Co-ZIF-8-800 catalyst was subjected to comprehensive post-reaction characterizations. High-resolution TEM (HRTEM), elemental mapping, and ICP-OES analyses exclude cobalt aggregation or leaching (Fig. S11 and Table S12 in the ESM). XANES and EXAFS analyses (Fig. S12 in the ESM) further reveal a slight increase in the Co–N coordination number (4.5 vs. 3.6) (Table S7 in the ESM), while the Zn–N coordination environment remains nearly unchanged (4.1 vs. 4.0) (Table S8 in the ESM). These results indicate that although the atomic dispersion of cobalt and the overall coordination framework are largely preserved, subtle evolution in the local Co–N coordination environment may modify the electronic and geometric properties of the active sites, thereby contributing to catalyst deactivation. Consistent with these observations, XRD result indicated that the used Co-ZIF-8-800 catalyst retained its characteristic peaks, suggesting structural stability (Fig. S13 in the ESM). However, the Brunauer–Emmett–Teller (BET) analysis revealed reduced surface area (Table S13 in the ESM), suggesting that the active Co-N_4 matrix was likely concealed during recycling. Collectively, these results suggest that the catalyst deactivation originates from a combination of local coordination evolution of Co sites and reduced surface accessibility, rather than irreversible structural degradation or metal loss. Notably, adding trace cobalt precursor (0.01 wt.% Co) to the used catalyst followed by re-pyrolysis can fully recover the activity, further confirming that trace cobalt species are essential for the catalytic performance.

The applicability of the Co-ZIF-8-800 catalyst was evaluated through a substrate scope study (Table 2). For the CTH of 5-hydroxymethylfurfural (HMF), which contains an additional –CH_2OH group, both the conversion and yield were relatively low (Table 2, entry 2). In contrast, a –CH_3 on the ring gave a similar conversion but a slightly lower yield (Table 2, entry 3). The reactivities of aromatic molecules with a phenolic or primary –OH group and a –CHO group (Table 2, entries 4 and 5) were again inferior. Thus, the negative impact of acidic H atoms previously identified in the substrates was also observed for the Co catalyst [14]. Compared with the hydrogen donor 2-propanol, the more acidic H atoms in primary hydroxyl or phenolic –OH groups can interact with the active centers of the Co-N_4 matrix, thereby suppressing the CTH activity. In contrast, benzaldehyde achieved a conversion of 95.4% and a benzyl alcohol yield of 84.0% (Table 2, entry 6). *p*-Substituted benzaldehydes with –F and –CF_3 produced slightly lower yields, while –Cl led to lower selectivity (Table 2, entries 7–9). The CTH reaction was greatly suppressed with the *p*-substituted *t*-butyl group, probably due to the steric effect, inhibiting the adsorption of the substrate (Table 2, entry 10). The lower reactivity of 2-phenylacetaldehyde suggests that its –CHO group is less reactive than the benzylic –CHO group (Table 2, entry 11). In contrast, an unsaturated aldehyde, like cinnamaldehyde, displayed higher reactivity (Table 2, entry 12). Substituting furan with thiophene slightly decreased the yield, while pyridine substitution led to a much lower yield (Table 2, entries 13 and 14). Overall, the catalyst exhibited high selectivity toward –CHO groups without ring hydrogenation, although its performance varied according to the structural features of the substrate, as anticipated.

4 Conclusions

In this study, we developed a Co-ZIF-8-800 catalyst with ultra-low cobalt loading (0.08 wt.%) for the CTH of FF to FFA using 2-PrOH as the hydrogen donor. Co-ZIF-8-800 outperformed other MOF-derived catalysts, achieving an FF conversion of 100% and an FFA selectivity of 96.5% under optimal conditions. Additionally, Co-ZIF-8-800 exhibited an exceptionally high TOF of 1290.6 h^{-1} at 120 °C, which is three to four orders of magnitude greater than those reported for other single Co catalysts. This remarkable activity is primarily attributed to the uniformly distributed Co–N_4 coordination environment and the presence of abundant weak and moderate acid sites. The substrate scope is also successfully expanded, highlighting its versatility for the transformation of various biomass-derived molecules.

Electronic Supplementary Material: Supplementary material (AC-TEM images, TEM images, XPS spectra, XRD patterns, NH_3-TPD profiles, XAFS spectra with corresponding fitting results, ICP analysis, BET analysis, and catalyst performance comparison) is available in the online version of this article at https://doi.org/10.26599/NR.2026.94908390.

Table 2 CTH of various aldehydes over Co-ZIF-8-800 catalyst[a]

Entry	Aldehyde substrate	*T* (°C)	*t* (h)	Conv. (%)	Product	Yield (%)[b]	Sel. (%)
1		120	6	> 99.9		96.5	96.5
2	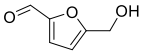	120	6	16.5	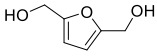	12.3	74.5
3	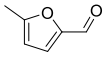	120	6	85.5	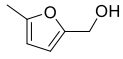	71.2	83.2
4	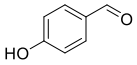	120	6	23.5	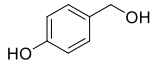	3.5	14.9
5	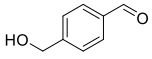	120	6	37.6	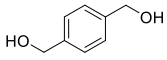	28.7	76.3
6	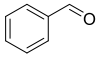	120	6	95.4	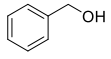	84.0	88.1
7	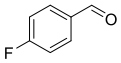	120 160	6 0.5	> 99.9 > 99.9	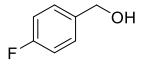	90.6 89.5	90.6 89.5
8	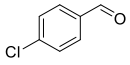	120 160	6 6	23.0 99.8	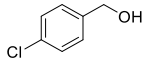	10.9 64.7	47.4 64.8
9	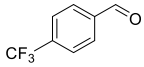	120	6	96.6	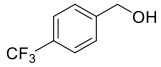	80.4	83.2
10	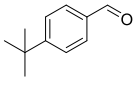	160	6	28.3	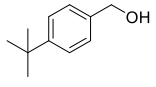	21.2	74.5
11	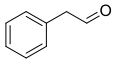	140 160	6 6	99.7 > 99.9	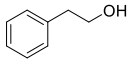	63.6 74.2	63.8 74.2
12	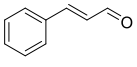	140 160	6 6	59.5 71.8	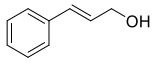	43.8 50.3	73.6 70.1
13		140	6	98.1	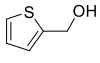	91.1	92.9
14		160	6	96.6	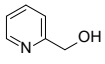	74.9	77.5

[a]Reaction conditions: 0.5 mmol of substrate, 3 mL of 2-PrOH, 50 mg of Co-ZIF-8-800 catalyst, *T* = 120 °C, and *t* = 6 h.

[b]GC yield.

Data availability

All data needed to support the conclusions in the paper are presented in the manuscript and the Electronic Supplementary Material. Additional data related to this paper may be requested from the corresponding author upon request.

Acknowledgements

This work was granted by the National Key Research and Development Program of China (Nos. 2024YFF0508700 and 2022YFB3506200), the National Natural Science Foundation of China (Nos. 22478424, 21702227, and 22122113), and the Science Foundation of China University of Petroleum, Beijing (No. 2462025QNXZ008).

Declaration of competing interest

All the contributing authors report no conflict of interests in this work.

Author contribution statement

J. L.: Project administration, writing manuscript, experimental design, funding acquisition. Z. X. L.: Project administration, writing manuscript, experimental design, funding acquisition. X. J. W: Data curation, writing manuscript, validation. Z. D. A.: Project administration, writing manuscript, experiments. T. W.: Project administration, experimental design, writing manuscript, experiments. J. X. L.: experimental design, experiments, validation. J. J. Z: experimental design, experiments, validation. All the authors have approved the final manuscript.

Use of AI statement

None.

References

[1] Alonso, D. M.; Bond, J. Q.; Dumesic, J. A. Catalytic conversion of biomass to biofuels. *Green Chem.* **2010**, *12*, 1493–1513.

[2] McKendry, P. Energy production from biomass (part 1): Overview of biomass. *Bioresour. Technol.* **2002**, *83*, 37–46.

[3] Liang, Z.; Song, L. P.; Sun, M. Z.; Huang, B. L.; Du, Y. P. Atomically dispersed indium and cerium sites for selectively electroreduction of CO_2 to formate. *Nano Res.* **2023**, *16*, 8757–8764.

[4] Li, Q. Q.; Sun, C.; Sun, X. L.; Yin, Z. J.; Du, Y. P.; Liu, J. C.; Luo, F. Synthesis of palladium-rare earth alloy as a high-performance bifunctional catalyst for direct ethanol fuel cells. *Nano Res.* **2024**, *17*, 9525–9531.

[5] Mamman, A. S.; Lee, J. M.; Kim, Y. C.; Hwang, I. T.; Park, N. J.; Hwang, Y. K.; Chang, J. S.; Hwang, J. S. Furfural: Hemicellulose/xylosederived biochemical. *Biofuel. Bioprod. Biorefin.* **2008**, *2*, 438–454.

[6] Yan, K.; Wu, G. S.; Lafleur, T.; Jarvis, C. Production, properties and catalytic hydrogenation of furfural to fuel additives and value-added chemicals. *Renew. Sustain. Energy Rev.* **2014**, *38*, 663–676.

[7] Hoydonckx, H. E.; Van Rhijn, W. M.; Van Rhijn, W.; De Vos, D. E.; Jacobs, P. A. Furfural and derivatives. In *Ullmann's Encyclopedia of Industrial Chemistry*. Wiley-VCH, Ed.; Wiley-VCH: Weinheim, 2007; pp 285–313.

[8] Nagaraja, B. M.; Padmasri, A. H.; David Raju, B.; Rama Rao, K. S. Vapor phase selective hydrogenation of furfural to furfuryl alcohol over Cu-MgO coprecipitated catalysts. *J. Mol. Catal. A: Chem* **2007**, *265*, 90–97.

[9] Li, J.; Liu, J. L.; Zhou, H. J.; Fu, Y. Catalytic transfer hydrogenation of furfural to furfuryl alcohol over nitrogen-doped carbon-supported iron catalysts. *ChemSusChem* **2016**, *9*, 1339–1347.

[10] Cho, H. J.; Kim, D.; Xu, B. J. Selectivity control in tandem catalytic furfural upgrading on zeolite-encapsulated Pt nanoparticles through site and solvent engineering. *ACS Catal.* **2020**, *10*, 4770–4779.

[11] Puthiaraj, P.; Kim, K.; Ahn, W. S. Catalytic transfer hydrogenation of bio-based furfural by palladium supported on nitrogen-doped porous carbon. *Catal. Today* **2019**, *324*, 49–58.

[12] Gilkey, M. J.; Panagiotopoulou, P.; Mironenko, A. V.; Jenness, G. R.; Vlachos, D. G.; Xu, B. J. Mechanistic insights into metal lewis acid-mediated catalytic transfer hydrogenation of furfural to 2-methylfuran. *ACS Catal.* **2015**, *5*, 3988–3994.

[13] Fan, Y. F.; Zhuang, C. F.; Li, S. J.; Wang, Y.; Zou, X. Q.; Liu, X. T.; Huang, W. M.; Zhu, G. S. Efficient single-atom Ni for catalytic transfer hydrogenation of furfural to furfuryl alcohol. *J. Mater. Chem. A* **2021**, *9*, 1110–1118.

[14] An, Z. D.; Yang, P. P.; Duan, D. L.; Li, J.; Wan, T.; Kong, Y.; Caratzoulas, S.; Xiang, S. T.; Liu, J. X.; Huang, L. et al. Highly active, ultra-low loading single-atom iron catalysts for catalytic transfer hydrogenation. *Nat. Commun.* **2023**, *14*, 6666.

[15] Zhai, Z. X.; Chu, J.; Sun, L.; Zhao, X.; Huang, D. J.; Yang, X. Q.; Zhuang, C. F.; Min, C. G.; Wang, Y. Ultrahigh metal content carbon-based catalyst for efficient hydrogenation of furfural: The regulatory effect of glycerol. *ACS Appl. Mater. Interfaces* **2022**, *14*, 44439–44449.

[16] Jiang, S. S.; Li, F.; Huang, J.; Wang, Y.; Lu, S. Y.; Li, P.; Li, C. Q. Catalytic transfer hydrogenation of furfural over magnetic carbon-encapsulated CoO@C catalyst. *ChemistrySelect* **2020**, *5*, 9883–9892.

[17] Yang, C.; Yao, J. S.; Meng, S. Y.; Wang, P.; He, M.; Li, P. G.; Xiao, P.; Xiao, J. Y.; Liu, Y. P.; Li, Z. X. A library of polymetallic alloy nanotubes: From binary to septenary. *J. Am. Chem. Soc.* **2025**, *147*, 9865–9878.

[18] Huai, M. B.; Li, X. M.; Zhang, Y.; Qin, X. M.; Zhang, Y. F.; Qin, X. Y.; Liu, Y. F.; Liang, X. X.; Li, G.; Zhao, J. B. Boosting furfural hydrogenation performance of confined co-based composites derived from ZIF-67 via a surfactant-assisted pyrolysis strategy. *ChemCatChem* **2025**, *17*, e202401651.

[19] Wang, F.; Zhang, Z. H. Catalytic transfer hydrogenation of furfural into furfuryl alcohol over magnetic γ-Fe_2O_3@HAP catalyst. *ACS Sustainable Chem. Eng.* **2017**, *5*, 942–947.

[20] Xiao, P.; Zhu, J. J.; Zhao, D.; Zhao, Z.; Zaera, F.; Zhu, Y. J. Porous $LaFeO_3$ prepared by an *in situ* carbon templating method for catalytic transfer hydrogenation reactions. *ACS Appl. Mater. Interfaces* **2019**, *11*, 15517–15527.

[21] An, Z. D.; Li, J. Recent advances in the catalytic transfer hydrogenation of furfural to furfuryl alcohol over heterogeneous catalysts. *Green Chem.* **2022**, *24*, 1780–1808.

[22] Ramos, R.; Peixoto, A. F.; Arias-Serrano, B. I.; Soares, O. S. G. P.; Pereira, M. F. R.; Kubička, D.; Freire, C. Catalytic transfer hydrogenation of furfural over Co_3O_4-Al_2O_3 hydrotalcite-derived catalyst. *ChemCatChem* **2020**, *12*, 1467–1475.

[23] Wang, J. L.; Ren, L. X.; Kong, Y.; Shuang, Y. Z.; Ye, Q.; Hong, C. X.; Wang, S. Y.; Ma, Z. L.; Wang, F.; Jian, J. et al. Laser derived Co_1Ni_1@MOF with efficient charge exchanges boosting selective catalytic hydrogenation. *Adv. Funct. Mater.* **2025**, *35*, 2421357.

[24] He, M.; Wang, P.; Yao, J. S.; Li, Y. F.; Meng, S. Y.; Li, Z. X. Lanthanum-based nanomaterials for oxygen evolution reaction. *J. Rare Earths* **2025**, *43*, 1091–1099.

[25] Nasiruzzaman Shaikh, M.; Ali, M.; Abdelnaby, M. M.; Hakeem, A. S.; Sanhoob, M.; Alghamdi, H. S.; Ajeebi, A. M.; Aziz, M. A. Facile hydrogenation of furfural by MOF-derived graphitic carbon wrapped FeCo bimetallic catalysts. *Chem.—Asian J.* **2023**, *18*, e202201254.

[26] Fan, Y. F.; Li, S. L.; Wang, Y.; Zhuang, C. F.; Liu, X. T.; Zhu, G. S.; Zou, X. Q. Tuning the synthesis of polymetallic-doped ZIF derived materials for efficient hydrogenation of furfural to furfuryl alcohol. *Nanoscale* **2020**, *12*, 18296–18304.

[27] Wu, J.; Yan, X. Y.; Wang, W. R.; Jin, M.; Xie, Y. H.; Wang, C. B. Highly dispersed CoNi alloy embedded in N-doped graphitic carbon for catalytic transfer hydrogenation of biomass-derived furfural. *Chem.—Asian J.* **2021**, *16*, 3194–3201

[28] Kang, R.; Wang, S.; Guo, D. Y.; Feng, J. F.; Pan, H. Trimetallic NiZr/CoO_x catalyst for the selective hydrogenation of furfural into furfuryl alcohol. *Int. J. Hydrogen Energy* **2024**, *51*, 1471–1482.

[29] Chen, J. Y.; Xiao, Y.; Guo, F. S.; Li, K. M.; Huang, Y. B.; Lu, Q. Single-atom metal catalysts for catalytic chemical conversion of biomass to chemicals and fuels. *ACS Catal.* **2024**, *14*, 5198–5226.

[30] De, S.; Burange, A. S.; Luque, R. Conversion of biomass-derived feedstocks into value-added chemicals over single-atom catalysts. *Green Chem.* **2022**, *24*, 2267–2286.

[31] Yao, Y. G.; Huang, Z. N.; Xie, P. F.; Wu, L. P.; Ma, L.; Li, T. Y.; Pang, Z. Q.; Jiao, M. L.; Liang, Z. Q.; Gao, J. L. et al. High temperature shockwave stabilized single atoms. *Nat. Nanotechnol.* **2019**, *14*, 851–857.

[32] Liu, Y. W.; Li, Z.; Yu, Q. Y.; Chen, Y. F.; Chai, Z. W.; Zhao, G. F.; Liu, S. J.; Cheong, W. C.; Pan, Y.; Zhang, Q. H. et al. A general strategy for fabricating isolated single metal atomic site catalysts in Y zeolite. *J. Am. Chem. Soc.* **2019**, *141*, 9305–9311.

[33] Yin, P. Q.; Yao, T.; Wu, Y. E.; Zheng, L. R.; Lin, Y.; Liu, W.; Ju, H. X.; Zhu, J. F.; Hong, X.; Deng, Z. X. et al. Single cobalt atoms with precise N-coordination as superior oxygen reduction reaction catalysts. *Angew. Chem., Int. Ed.* **2016**, *55*, 10800–10805.

[34] Liu, G. L.; Robertson, A. W.; Li, M. M. J.; Kuo, W. C. H.; Darby, M. T.; Muhieddine, M. H.; Lin, Y. C.; Suenaga, K.; Stamatakis, M.; Warner, J. H. et al. MoS_2 monolayer catalyst doped with isolated Co atoms for the hydrodeoxygenation reaction. *Nat. Chem.* **2017**, *9*, 810–816.

[35] Ji, S. F.; Chen, Y. J.; Wang, X. L.; Zhang, Z. D.; Wang, D. S.; Li, Y.

D. Chemical synthesis of single atomic site catalysts. *Chem. Rev.* **2020**, *120*, 11900–11955.

[36] Cravillon, J.; Münzer, S.; Lohmeier, S. J.; Feldhoff, A.; Huber, K.; Wiebcke, M. Rapid room-temperature synthesis and characterization of nanocrystals of a prototypical zeolitic imidazolate framework. *Chem. Mater* **2009**, *21*, 1410–1412.

[37] Yin, L. L.; Zhang, S.; Sun, M. Z.; Wang, S. Y.; Huang, B. L.; Du, Y. P. Non-bonding modulations between single atomic cerium and monodispersed selenium sites towards efficient oxygen reduction. *Nano Res.* **2024**, *17*, 4753–4763.

[38] Tong, M. M.; Sun, F. F.; Xie, Y.; Wang, Y.; Yang, Y. Q.; Tian, C. G.; Wang, L.; Fu, H. G. *Operando* cooperated catalytic mechanism of atomically dispersed Cu-N_4 and Zn-N_4 for promoting oxygen reduction reaction. *Angew. Chem. , Int. Ed.* **2021**, *60*, 14005–14012.

[39] An, Q. Z.; Qin, X. P.; Sun, X.; Zhang, X.; Zhang, Y. H.; Guo, J. L.; Jiang, J. J.; Zhang, J.; Li, B. J.; Jiang, Y. L. et al. *In situ* identification of zinc sites as potential-dependent selectivity switch over dual-atom catalysts for H_2O_2 electrosynthesis. *J. Am. Chem. Soc.* **2025**, *147*, 11465–11476.

[40] Wang, Q.; Ina, T.; Chen, W. T.; Shang, L.; Sun, F. F.; Wei, S. H.; Sun-Waterhouse, D.; Telfer, S. G.; Zhang, T. R.; Waterhouse, G. I. N. Evolution of Zn(II) single atom catalyst sites during the pyrolysis-induced transformation of ZIF-8 to N-doped carbons. *Sci. Bull.* **2020**, *65*, 1743–1751.

[41] Lin, L.; Liu, T. F.; Xiao, J. P.; Li, H. F.; Wei, P. F.; Gao, D. F.; Nan, B.; Si, R.; Wang, G. X.; Bao, X. H. Enhancing CO_2 electroreduction to methane with a cobalt phthalocyanine and zinc-nitrogen-carbon tandem catalyst. *Angew. Chem., Int. Ed.* **2020**, *59*, 22408–22413.

[42] Huang, Z. J.; Wu, J.; Yan, F. W.; Yuan, G. Q. MOF-derived single-atom catalysts with dense zinc and nitrogen sites for efficient CO_2 cycloaddition. *Catal. Sci. Technol.* **2025**, *15*, 2286–2294.

[43] Yang, J. Y.; Huang, Y. K.; Qi, H. F.; Zeng, C. B.; Jiang, Q. K.; Cui, Y. T.; Su, Y.; Du, X. R.; Pan, X. L.; Liu, X. Y. et al. Modulating the strong metal–support interaction of single-atom catalysts via vicinal structure decoration. *Nat. Commun.* **2022**, *13*, 4244.

[44] Liu, Z. H.; Zhang, Z. Z.; Wen, Z.; Xue, B. High efficiency catalytic transfer hydrogenation of furfural to furfuryl alcohol over metallic oxide catalyst. *Catal. Lett.* **2022**, *152*, 3537–3547.